Atomic scale simulations of 112 symmetric incoherent twin boundaries in gold

Yen Fred Woguem, Pierre Godard, Julien Durinck, Sandrine Brochard

Atomic Scale Simulations of {112} Symmetric Incoherent Twin Boundaries in Gold

Yen Fred Woguem*, Pierre Godard, Julien Durinck, Sandrine Brochard

Université de Poitiers, ISAE-ENSMA, CNRS, PPRIME, Poitiers, France

Abstract

The crystalline defects may play an important role in the improvement of the properties of materials. This is the case of twin boundaries which improve the mechanical properties. $\Sigma3\{111\}$ coherent twin boundaries (CTBs) and $\Sigma3\{112\}$ symmetric incoherent twin boundaries (ITBs) are two defects studied in this work. Atomistic simulations with four interatomic potentials commonly used in the literature and density functional theory have been used to characterize in detail these two defects in gold. The results show that the excess volumes introduced by twin boundaries strongly depend on the potential. After the ITB relaxation, a portion of 9R phase is formed. This phase is rotated from the face centred cubic (fcc) phase through an angle α which has been determined. The 9R phase formation energy γ_{form} has been quantified through atomic scale simulations. We put forward a model to calculate this formation energy γ_{form} as a function of the intrinsic stacking fault energy γ_{ISF} and the excess volume. This model shows that the interaction energy between ISFs is much larger for the Ackland and Baskes potentials than for the Foiles and Grochola potentials. Furthermore, the elastic deformation ε_{xx} produced in the system to ensure consistency between the 9R phase and the fcc phase is computed. It allows us to discuss the width of the 9R phase in terms of γ_{form} and elastic energy and not uniquely in terms of γ_{ISF}, as previously done in the literature.

Keywords: Twin boundary, Atomistic simulation, Excess volume, 9R phase

1. Introduction

When defects are introduced into materials, their mechanical and electrical properties change. In recent years, Lu and co-workers have shown that nanotwinned metals have mechanical properties that are usually antagonistic, namely high yield strength and good ductility, without degrading the electrical conductivity [1, 2]. The association of these properties has also been observed by Anderoglu et al. [3]. Atomic scale simulations have shown that the yield strength of twinned gold or copper nanowires of finite length during deformation depends on the distance between coherent twin boundaries (CTBs) [4, 5].

The energy dependence on the inclination of $\Sigma3$ or other grain boundaries has been determined, clearly showing local minima for particular angles [6, 7, 8, 9]. Recent works have studied a large set of $\Sigma3$ grain boundaries and found that they facet into one of the three low energy boundary planes, {111}, {211} and {101} [10, 11, 12]. In the present study, we focus on $\Sigma3\{111\}$ coherent and $\Sigma3\{112\}$ symmetric incoherent twin boundaries (ITBs).

$\Sigma3\{112\}$ ITBs have been observed experimentally with transmission electron microscopy [13, 14, 15, 16, 17]. Using high resolution transmission electron microscopy (HRTEM), it has been shown in gold, palladium, silver and copper that the dissociation of the ITB may produce a hexagonal phase called 9R phase [6, 13, 15, 16, 17, 18, 19, 20, 21, 22, 23, 24, 25, 26]. The appearance of this phase has been confirmed by atomic scale simulations [13, 14, 18]. The formation of the 9R phase from the undissociated ITB has been explained by the glide of Shockley partial dislocations [17, 20]. This mechanism has also been observed by atomistic simulations and it has been shown that, under an applied shear, an ITB reacts by expanding the 9R phase through the motion of edge Shockley partial dislocations [17, 20, 26, 27]. ITB migration has also been studied [13, 27].

Wang and co-workers have studied the effect of the intrinsic stacking fault energy γ_{ISF} on the width of the 9R phase. In their atomic scale calculations, they have considered different face centred cubic (fcc) metals (Ag, Cu, Pd and Al), each having different γ_{ISF} values. They have noticed that the width of the 9R phase decreases when the intrinsic stacking fault energy increases [28]. Gu and co-workers have studied experimentally the effect of the stacking fault energy on the split (or dissociation) length of the 9R phase in coarse-grained Cu-Al alloys using HRTEM. They have observed that, when γ_{ISF} increases, the maximum split length of the 9R phase increases [29]. Though those previous works both indicate that the width of the 9R phase depends on γ_{ISF}, their seemingly contradictory results highlight that this dependence is not so obvious. This controversy also suggests that it is worth checking if the width of the 9R phase depends only on γ_{ISF} or on

*Corresponding author, email address: yen.fred.woguem@univ-poitiers.fr

other parameters such as the formation energy of the 9R phase [18, 30] and/or the elastic deformation produced in the system to ensure consistency between the 9R and the fcc phases [18].

In this work, we have used molecular static (MS) simulations in order to characterize the $\Sigma3\{111\}$ CTB, $\Sigma3\{112\}$ ITB and the 9R phase in gold with four interatomic potentials commonly used in the literature and the density functional theory (DFT) method. This provides different estimations of several parameters, such as the intrinsic staking fault energy, for the same material. In order to study their influence on the width of the 9R phase ensuing from the ITB relaxation, we have determined the 9R phase formation energy and the elastic deformation produced in the system to ensure consistency between the 9R and the fcc phases for these four potentials and DFT calculations. We have also developed a model to highlight the parameters that influence the 9R phase formation energy, and compared the obtained values with the simulation results. This paper is organized as follows: the model, methods and bulk properties of each phases are detailed in section II, in section III we present the results of the TBs relaxations, and the characteristics of the 9R phase in a relaxed ITB are then discussed in section IV.

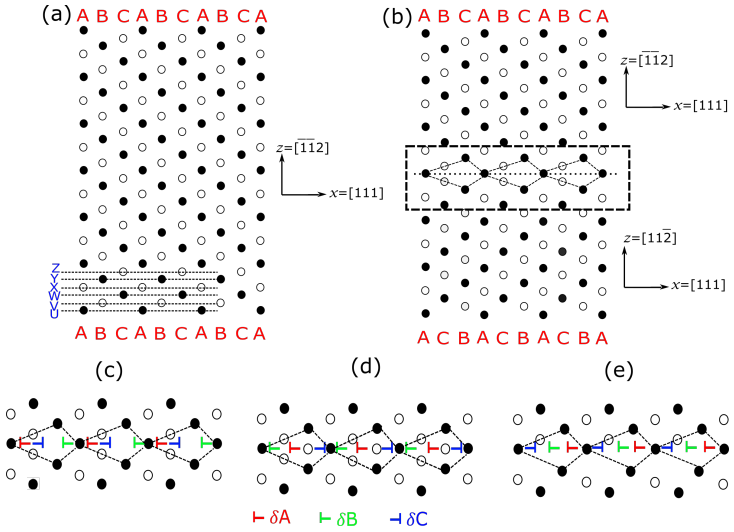

Figure 1: Atomic structure viewed along $[1\bar{1}0]$ of (a) a perfect fcc crystal and (b) a crystal with a $\Sigma3(11\bar{2})$ type I ITB before relaxation. The stacking sequences are indicated by letters, ABC and UVWXYZ, along [111] and $[11\bar{2}]$ directions, respectively. In b) the position of the twin boundary plane is indicated by a dotted line and the zoomed zone by a dashed line. c-e) Zooms on different ITB types viewed along $[1\bar{1}0]$: c) type I, d) type III and e) type IV. The structural units and the ITB description with Shockley partial dislocations are highlighted.The different shadings correspond to the position of the atoms along $[1\bar{1}0]$, equal to zero or $a_{0c}\sqrt{2}/4$ (a_{0c} being the lattice parameter of the fcc crystal).

2. Models and Methods

2.1. Studied systems

For this study, we first considered $\Sigma3(111)$ CTB and $\Sigma3(11\bar{2})$ ITB in an fcc crystal. Both TBs can be constructed by tilt operations: the CTB by cutting the crystal along a (111) plane and performing a 180° rotation of one part around the $[11\bar{2}]$ direction, and the ITB by cutting the crystal along a $(11\bar{2})$ plane and performing a 180° rotation of one part around the [111] direction. However, the detailed atomic structure of $\Sigma3\{112\}$ ITBs is much more complex than that of a CTB, and can be considered in several ways, as shown in figure 1. The type I ITB structure, as labeled by Wang et al [26], is shown in figure 1b and 1c. It is obtained from the dichromatic pattern and an appropriate choice of the cutting (boundary) plane. It can also be described by a set of three Shockley partial dislocations δA, δB, δC, one partial on every (111) plane [17, 20]. The repeatable sequence is $\delta A : \delta C : \delta B$, where δC is a pure edge dislocation with a Burgers vector $1/6[11\bar{2}]$, δA and δB are mixed dislocations with the same edge component and opposite screw components; their Burgers vectors are respectively $1/6[1\bar{2}1]$ and $1/6[\bar{2}11]$.

The atomic structure of the type I ITB discussed above is not the only one that can be obtained for a $\Sigma3(11\bar{2})$ symmetric ITB. First, by selecting a different cutting plane in the dichromatic pattern, or by using a different set of partial dislocations (δC:$-2\delta C$:δC), one gets the type II ITB [26]. This type II ITB is not considered here, because Wang et al have shown that, after relaxation, though it is stable energetically, it has a larger boundary energy and should be less prevalent than the type I ITB [26]. Second, with the same set $\{\delta A, \delta B, \delta C\}$ of partial dislocations as for the type I ITB, but shifting the glide planes, two other ITB atomic structures are obtained, as shown in figure 1d and 1e. We call them type III for the $\delta B : \delta A : \delta C$ partial dislocations sequence and type IV for the $\delta C : \delta B : \delta A$ sequence (note that the glide plane reference is fixed for the first dislocation of the sequence). Figure 2 shows the detailed formation mechanism of the type III ITB from a perfect fcc crystal by the successive glide of the repeatable set of partial dislocations.

For classical MS calculations, the numbers of (111), $(1\bar{1}0)$ and $(11\bar{2})$ atomic planes in the computation cell for the ITB study are respectively 18, 12 and 216. The corresponding figures for the study on the CTB are 216, 24 and 24. We call the directions $x//[111]$, $y//[1\bar{1}0]$ and $z//[11\bar{2}]$. Free surfaces limit the system along the normal to the twin boundary, while periodic boundary conditions are used along the orthogonal directions.

Due to the high numerical cost inherent to DFT calculations in comparison to classical MS simulations, the computational cell for the configuration including the ITB is more limited in size with 9, 2 and 60 (111), $(1\bar{1}0)$ and $(11\bar{2})$ planes respectively. The computational cell for the CTB is built with basis vectors along the [110], $[\bar{1}10]$ and [111] with 2, 2 and 19 atomic planes along these three crystal directions respectively. 3D periodic boundary conditions are considered with a vacuum thickness of 14 Å along the normal to the twin boundaries in order to prevent interac-

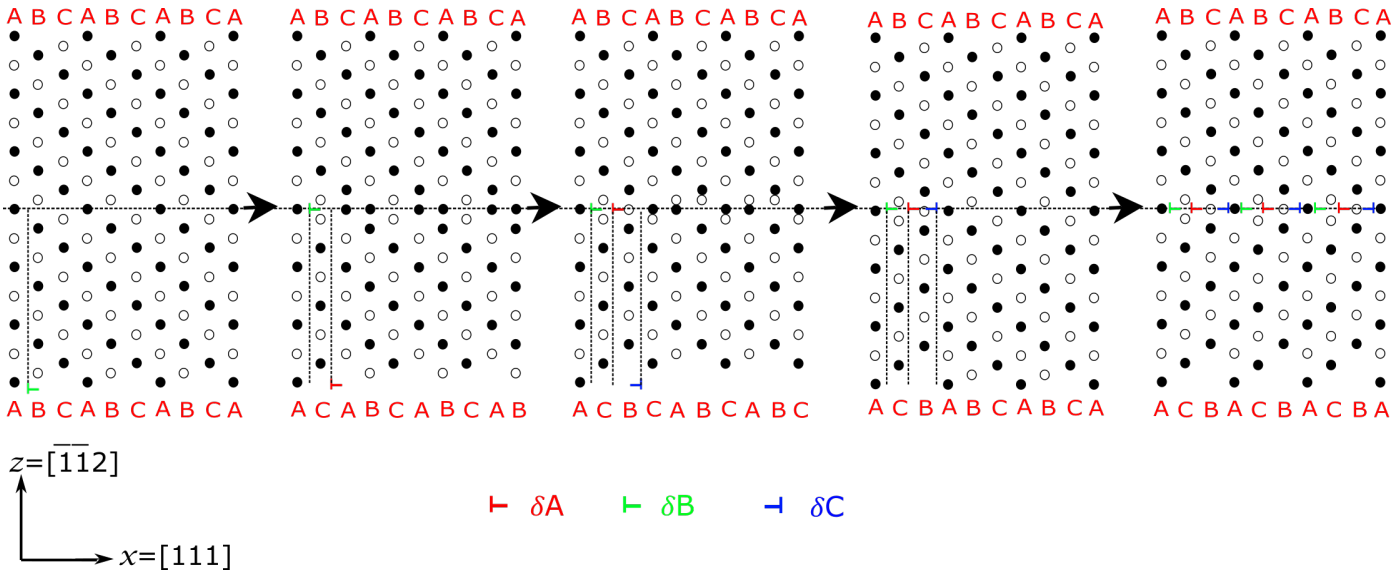

Figure 2: Glide of the set of partial dislocations to form the type III ITB.

tions between the periodic images of the system.

2.2. Methods

For classical MS calculations, we have used the LAMMPS (Large-Scale Atomic/Molecular Massively Parallel Simulator) code [31] with the embedded-atom method (EAM) interatomic potentials of Foiles [32], Grochola [33] and Ackland [34], and the modified embedded-atom method (MEAM) potential of Baskes [35]. Relaxation of the model has been done using the Hessian-free truncated Newton algorithm at 0 K. All atom positions are relaxed fully and independently until all the force components on any atom do not exceed 10^{-4} eV/Å.

DFT caculations are performed using the VASP (Vienna Ab initio Simulation Package) code [36, 37, 38], within the Generalized Gradient Approximation (GGA) framework parametrized by Perdew, Burke and Ernzerhof (PBE) [39] but also within the Local Density Approximation (LDA) framework. The interactions between ions (core electrons and atom nucleus) and valence electrons are described by the Projector Augmented Wave (PAW) pseudopotential formalism [40]. A Monkhorst-Pack sampling of the irreducible Brillouin zone is used with 20×20×20 k-points for the primitive cell of the Au crystal (12×20×1 and 20×20×1 for the cells containing the ITB and the CTB, respectively). A cut-off energy equal to 400 eV is considered for the truncation of the plane-wave expansion of the electron basis set. The ground state charge density is calculated using the blocked Davidson iteration scheme and the position of the ions is optimized by a conjugate gradient algorithm until the total energy no longer varies by more than 10^{-4} eV.

The analyses of the obtained structures have been performed with the OVITO (Open Visualization Tool) software [41].

2.3. Bulk characteristics of the fcc and 9R phases

Some characteristics of the fcc phase in gold for the four potentials and the DFT are given and compared to experimental data in table 1. While all potentials show satisfactory values for the lattice parameter, the GGA-DFT overestimates it with a difference of 2.2% and the LDA-DFT slightly underestimates it. Compared to the experimental and DFT values, the intrinsic stacking fault energy γ_{ISF} is underestimated by Foiles, overestimated by Grochola and Baskes and accurately estimated by Ackland. The experimental stiffness coefficients are reproduced to 10% by the interatomic potentials and to 5-60% by DFT depending on whether LDA or GGA is considered. The best match to the experimental data is obtained by the Grochola potential and using the LDA for the classical and DFT calculations respectively. Indeed, the values of stiffness coefficients obtained using the LDA are closer to experimental ones than using the GGA, as already mentioned in [42].

A bulk system of 9R phase has been constructed (figure 3) and relaxed to calculate its cohesive energy $E_{coh,R}$, lattice parameters a_{0R} and c_{0R}, stiffness coefficients and bulk modulus. The results are given in table 2. To the best of our knowledge, there is no experimental data to compare with our numerical results for the 9R phase: indeed, this crystallographic structure does not seem to be stable in the bulk for gold. As such, a more rigourous term to describe the structure that appears at the ITB dissociation would be complexion rather than phase [46, 47]. Since the introduction of the notion of complexion in 2006 [46], an entire field, stemming from the complexions in ceramics and expanding into metallic systems, has been developing, to which our study might be related. However, all the complexion transitions studied in the literature and reviewed e.g. in [47] do not apply in our case. In this paper, we

	Foiles	Grochola	Ackland	Baskes	GGA	LDA	Experiment
a_{0c} (Å)	4.08	4.07	4.08	4.07	4.17	4.06	4.08 [43]
$E_{coh,c}$ (eV/atom)	-3.930	-3.924	-3.789	-3.929	NC	NC	
γ_{ISF} (mJ/m^2)	4.8	42.6	32.0	56.0	27.5	27.0	33 [44]
C_{11} (GPa)	180	201	186	188	148	211	202 [45]
C_{12} (GPa)	156	169	157	158	130	182	170 [45]
C_{44} (GPa)	45	46	42	43	20	38	45 [45]
B (GPa)	164	180	167	168	136	192	180 [45]

Table 1: Fcc gold lattice parameter a_{0c}, cohesive energy $E_{coh,c}$, intrinsic stacking fault energy γ_{ISF}, stiffness coefficients C_{11}, C_{12}, C_{44} and bulk modulus B obtained from the different interatomic potentials, DFT and experimental data. NC stands for Not Computed.

prefer the term 9R phase commonly used in the literature for decades. Note that in this paper, the $[0001]_h$ direction of the bulk hexagonal 9R phase is called $[111]_{9R}$ direction of the 9R phase, because the 9R phase can be considered as the stacking of nine (111) planes in an fcc phase with one intrinsic stacking fault every three planes (see figures 3). The values of the cohesive energies of the 9R and fcc phases have been computed for a bulk system.

3. Results and discussions

3.1. Twin boundaries relaxation

3.1.1. Relaxation of types I, III and IV ITBs and description of the 9R phase

We have determined the relaxed configurations and energies of the CTB and of types I, III and IV ITBs. For the four interatomic potentials, a portion of 9R phase is formed during the relaxation of the ITB, as shown in figure 4. For each potential, the atomic structure and energy obtained after relaxation are exactly the same regardless of the type of unrelaxed ITB (I, III, or IV) considered as the starting configuration. However, the atomic displacements are smaller during the relaxation of a $\Sigma3(11\bar{2})$ symmetric ITB when the glide of partial dislocations starts from a type III ITB, as shown in figure 5.

The 9R phase appears due to the glide of the pure edge partial dislocations δC, producing one intrinsic stacking fault every three planes, and thus the ABCBCACAB stacking. It can also be described using hexagonal (H) and fcc (C) planes by the CHHCHHCHH stacking. The array of Shockley partial dislocations between the 9R and the fcc phases induces a rotation of their (111) planes (figure 4.a); the theoretical angle is $\alpha = \arctan\left(\frac{1}{3\sqrt{2}}\right) \approx 13.26°$ [7].

The 9R phase was not clearly obtained during the relaxation of the ITB in our DFT calculations. In that case, the ITB relaxes in a configuration for which the δC edge dislocation seems to have hardly moved. We suspect that the reduced size of the system impedes the full formation of the 9R phase by promoting instead crystal rotations on either side of the ITB as an additional energy release mechanism (figures 4.e and f). But DFT calculations with larger systems are beyond the scope of this study.

3.1.2. Twin boundaries excess volume and energy

The introduction of a twin boundary in a previously perfect crystal may change its volume if the crystal size is free to relax. The excess volume is defined as this variation of volume per unit area of twin boundary [50, 51]. It represents the expansion or contraction along the normal to the TB. It will be denoted by δ_{CTB} or δ_{ITB} for CTBs or ITBs, respectively. To determine it, we consider two systems, one with a TB and free surfaces and another one with only surfaces, which is the reference system. The excess volume δ_{TB} is computed as $\delta_{TB} = \frac{l_{zf} - l_{z0}}{2}$ where l_{z0} is the relaxed length of the reference system and l_{zf} is the length of the relaxed system containing the twin boundary. The volume difference obtained for the whole system is divided by 2 to get the excess volume per grain, and it reduces to a length difference since it is normalized by the surface area of the twin boundary. The twin boundaries energies are obtained as the difference in energies of the two relaxed systems (crystal with the TB and reference system) divided by the twin boundary area. For all the potentials and our DFT calculations, the excess volume and energy values found for the CTB and the ITB are reported in table 3.

One can note that the values of the twin boundary excess volume and energy greatly depend on the potential. In modulus, the excess volume of the ITB is greater than or equal to the one of the CTB. The energy of the ITB is much larger than that of the CTB. The excess volume of the CTB is negative for the potentials of Foiles and Grochola and positive for the potentials of Ackland, Baskes and the DFT calculations. For the ITB, the excess volume is negative for the Grochola potential and positive in all other cases. We observe that the same effect as with DFT is obtained with the potentials of Ackland and Baskes for both the CTB and the ITB, while with the Foiles potential it is only for the ITB, and the Grochola potential gives signs in contrast with the DFT for both TBs. Among the different potentials, the one of Grochola gives the smaller δ_{CTB} but the larger γ_{CTB}, which was not expected. Indeed, a rough correlation between the excess volume and the energy of a grain boundary is established in the literature [8, 52]. In contrast to the CTB, our simulations with the four interatomic potentials exhibit a clear increase of γ_{ITB} with δ_{ITB}. We tested that the system size influ-

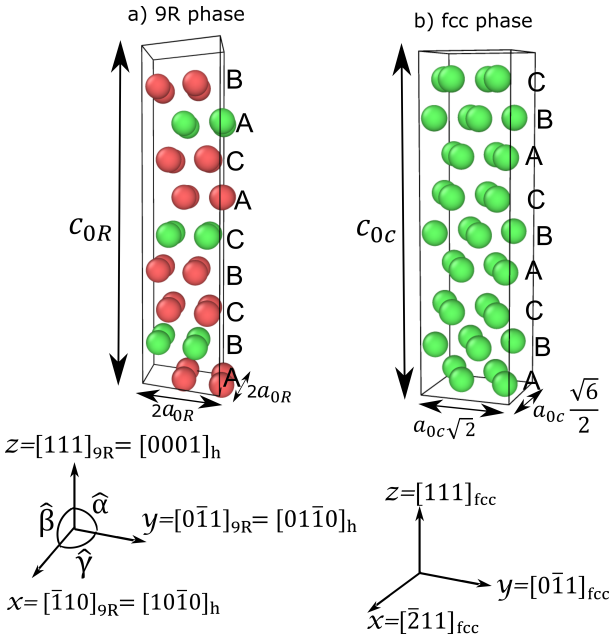

Figure 3: Representation of a) the hexagonal structure of the 9R phase and b) the fcc phase. $\widehat{\alpha} = 90°$, $\widehat{\beta} = 90°$ and $\widehat{\gamma} = 120°$ for the hexagonal structure. The coordinate system of figure b is orthogonal. $[hkl]_{9R}$ and $[hkl]_{fcc}$ refer to directions expressed in a cubic system for the 9R and fcc structures respectively whereas $[uvtw]_h$ refers to a hexagonal system. Atoms are colored according to the common neighbour analysis (CNA) parameter (characteristic of the local crystal structure around an atom [48, 49]): atoms in an fcc and a hexagonal crystal arrangement are respectively in green and red. The stacking sequences indicated by letters (ABC) refer to an fcc structure.

	Foiles	Grochola	Ackland	Baskes	GGA	LDA
a_{0R} (Å)	2.886	2.878	2.869	2.876	2.932	2.856
c_{0R} (Å)	21.18	21.12	21.49	21.24	22.00	21.37
$E_{coh,R}$ (eV/atom)	-3.929	-3.918	-3.785	-3.924	NC	NC
$C_{11,R}$ (GPa)	206	223	249	229	193	276
$C_{12,R}$ (GPa)	157	164	170	166	117	154
$C_{13,R}$ (GPa)	138	141	136	147	105	151
$C_{33,R}$ (GPa)	227	247	289	239	175	253
$C_{44,R}$ (GPa)	23	28	22	23	14	20
$C_{66,R}$ (GPa)	25	29	39	31	38	61
B_R (GPa)	167	176	186	180	NC	NC

Table 2: 9R gold lattice parameters a_{0R} and c_{0R}, cohesive energy $E_{coh,R}$, stiffness coefficients ($C_{ij,R}$) and bulk modulus (B_R) obtained from the different interatomic potentials and the DFT. NC stands for Not Computed.

	Foiles	Grochola	Ackland	Baskes	GGA	LDA
δ_{CTB} (Å)	-1.2 10^{-3}	-2.0 10^{-3}	5.8 10^{-3}	2.5 10^{-3}	6.1 10^{-3}	7.3 10^{-3}
δ_{ITB} (Å)	0.020	-0.002	0.180	0.060	0.061	0.039
γ_{CTB} (mJ/m^2)	2.4	21.3	17.3	20.2	15.3	14.0
γ_{ITB} (mJ/m^2)	386.9	371.1	580.8	438.3	223.8	320.4

Table 3: Excess volume δ_{TB} and energy γ_{TB} of CTBs and ITBs for the interatomic potentials and DFT.

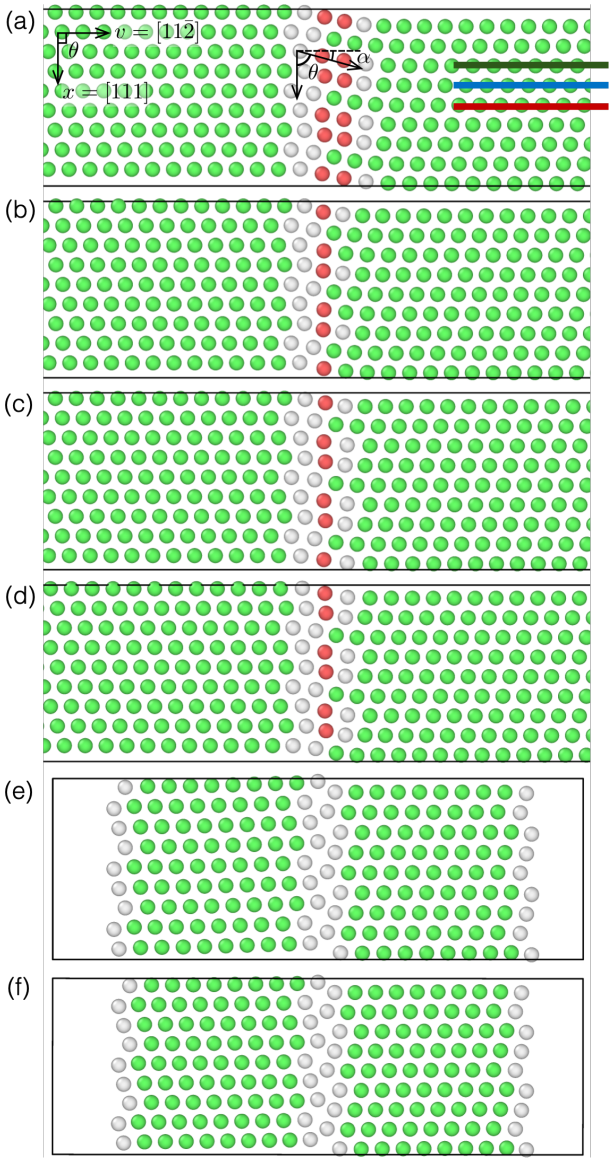

Figure 4: Relaxed ITB atomic structure with the potentials of a) Foiles, b) Grochola, c) Ackland, d) Baskes, and DFT calculations using (e) LDA and (f) GGA. Atoms are colored according to their CNA parameter: atoms in an fcc, a hexagonal and an unidentified crystal arrangement are respectively in green, red and white. α is the rotation angle of (111) atomic planes in the 9R phase and θ is the angle between the two basis vectors x and v. The green, blue and red lines correspond to the three different (111) planes considered to determine θ in subsection 3.2.1.

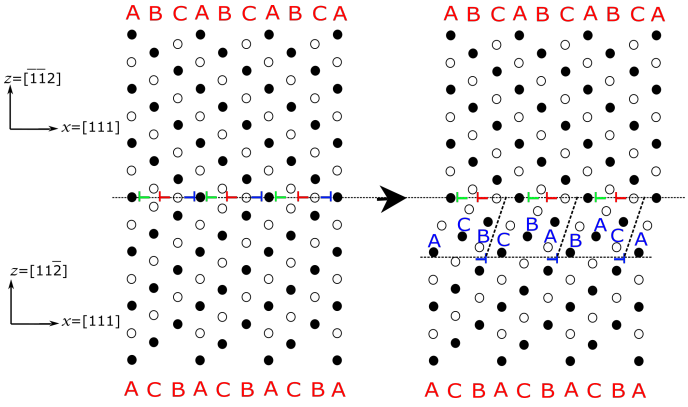

Figure 5: Slip of the pure edge partial dislocations δC yielding the 9R phase for a type III ITB.

ence on the computed excess volume values is weak: for example, the values of the excess volumes for the CTB determined with the Foiles potential are -1.179×10^{-3} and -1.181×10^{-3} Å for 108 and 432 layers, respectively.

3.2. The 9R phase in a relaxed Σ3{112} ITB

3.2.1. Width of the 9R phase

The width of the 9R phase obtained with classical MS has been determined using two methods, termed the angular method which is also accessible experimentally and the disregistry method which needs numerical simulations.

The angular method relies on the rotation of atomic planes in the 9R phase. We have determined the angle $\theta = 90° - \alpha$ between the x (the [111] direction of the fcc phase) and $v//[11\bar{2}]$ directions in each crystallographic phase (see figure 4). One obtains curves $\theta = f(z)$ (z being the coordinate along the $[11\bar{2}]$ direction in the fcc phase) for the three (111) planes of the 9R phase (HHC sequence). The results are shown in figure 6 for the Foiles potential. The first plane (in red) is in a fcc planes stacking, whereas the second (in blue) and third planes (in green) are in hexagonal close-packed stackings.

A threshold is chosen such that the 9R phase corresponds to a disorientation $\alpha > 3°$, or $\theta < 87°$. The width of the 9R phase is obtained using the mean of the extreme values stemming from the three curves corresponding to the three planes (see the inset in figure 6). The uncertainty is around 0.6 Å. The results obtained for the four potentials are given in table 4. Besides the 9R phase width, this method allows us to quantify the rotation of the (111) planes across the ITB. We have computed the maximum angle of disorientation α_m (average over the three planes), which values are also given in table 4. These values are straightforwardly compared with experiments since this method has been used to determine the width of the 9R phase on HRTEM images [15]. However, it strongly depends on the choice of the threshold; another method is thus proposed.

Since the 9R phase is delimited by the mixed dislocations on one side and the edge dislocations on the other

	Foiles	Grochola	Ackland	Baskes
e_{9R} (disregistry) (Å)	7.7	5.2	3.1	3.6
e_{9R} (angle) (Å)	9.9	7.2	7.0	6.9
α_m (degree)	10.92	12.05	8.40	11.30

Table 4: Width of the 9R phase obtained with the disregistry and angular methods and the maximum angle of disorientation α_m obtained with the angular method for the four interatomic potentials.

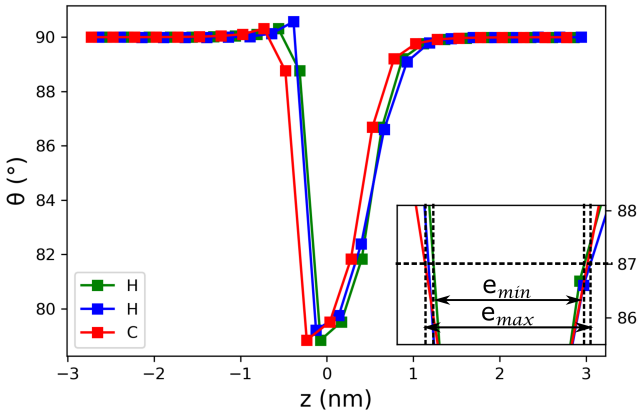

Figure 6: Line profile of the angle θ variation across the ITB for the Foiles potential. The three (111) planes of the HHC sequence correspond to the three lines in green, blue and red in figure 4.a. The inset shows how the extreme values of the width are determined.

side, we have considered the disregistry method which makes it possible to precisely determine the positions of these different dislocations. The disregistry is the evolution, after the glide of a dislocation in a plane, of the relative positions between pairs of atoms [26, 53]. The disregistry is calculated in the (111) glide planes of the δA, δB and δC dislocations, for pairs of atoms that are nearest neighbours on each side of the considered glide plane. It is decomposed into "edge" (along z) and "screw" (along y) components, denoted e.g. by (DAz, DAy) for the δA dislocation. In figure 7, the edge (respectively screw) component of the disregistry is adimensionalized with the norm of the edge (respectively screw) component of the mixed partial dislocations Burgers vectors. The width e_{9R} of the 9R phase has been determined using the edge component DCz of the disregistry in the glide plane of the δC dislocation (which is a pure edge dislocation), and the screw component of the disregistry DAy in the glide plane of the δA mixed dislocation. Two limits are used, as shown in figure 7a: the first one is at the position of the last point with a normalized disregistry value of 1 for DAy, the second one is the position of the δC dislocations cores, which is determined as the inflection point of the arctangent function used to fit DCz (red curve in figure 7b). The δC dislocations cores have also been localized with the DXA (Dislocation Extraction Algorithm) of OVITO (figure 7c); their positions are in excellent agreement with the disregistry analysis. The width of the 9R phase obtained for all the potentials with this procedure is given in table 4.

Note that we considered that the 9R phase was delimited by the edge dislocations δC and the mixed dislocations δA. This led e.g. to a width of 7.7 Å for the Foiles potential. Had we chosen the other mixed dislocations δB, we would have found 6.9 Å. However, this choice of a different criterion does not change the order of the potentials as far as the width is concerned. Also, this order is almost not changed when considering the angular method, with the largest width obtained for the Foiles potential, then the Grochola potential, and comparable widths for the Ackland and Baskes potentials.

3.2.2. Formation energy of the 9R phase

Classical molecular statics simulations give the cohesion energies $E_{coh,c}$ and $E_{coh,R}$ of the fcc and 9R phases, respectively (tables 1 and 2); the difference between these two terms is the formation energy of the 9R phase:

$$E_{form} = E_{coh,R} - E_{coh,c}. \quad (1)$$

The formation energy E_{form} has also been figured out from DFT calculations by taking the difference between the energies per atom of the bulk fcc phase and 9R phase.

In addition, the formation energy can also be apprehended with the following model. Let us consider a box with nine (111) planes of 9R phase. The energy of this system can be described in two ways: first, it is given by $E_1 = NE_{coh,R}$, with N the number of atoms in the box. Second, this system may also be defined as an fcc phase with one intrinsic stacking fault every three planes; the energy of the system is then given by $E_2 = NE_{coh,c} + 3S\gamma_{ISF} + S\gamma_{int-ISFs}$; S is the surface of the (111) planes and $\gamma_{int-ISFs}$ is the interaction energy between the ISFs per unit area of ISF. The volume of this box is, according to the first description, $V_1 = Nv_{9R}$ with v_{9R} the atomic volume in the 9R phase given by $v_{9R} = \frac{\sqrt{3}}{2}\frac{a_{0R}^2 c_{0R}}{9}$. According to the second description, the same volume is $V_2 = Sh$ with h the height of the box given by $h = 3\sqrt{3}a_{0c} + 12\delta_{CTB}$ (we use the fact that an ISF may be described as two CTBs on adjacent planes, and that each CTB introduces an excess volume of $2\delta_{CTB}$). Considering $E_1 = E_2$ and $V_1 = V_2$, the model leads to an estimation of the formation energy of the 9R phase:

$$E_{form}^{(mod)} = \left(\frac{v_{9R}}{\sqrt{3}a_{0c} + 4\delta_{CTB}}\right)\left(\gamma_{ISF} + \frac{\gamma_{int-ISFs}}{3}\right). \quad (2)$$

	Foiles	Grochola	Ackland	Baskes	GGA	LDA
E_{form} (eV/atom)	$7.1\,10^{-4}$	$6.4\,10^{-3}$	$4.1\,10^{-3}$	$5.9\,10^{-3}$	$3.3\,10^{-3}$	$3.1\,10^{-3}$
$E_{form}^{(mod)}$ (eV/atom)	$7.1\,10^{-4}$	$6.4\,10^{-3}$	$4.8\,10^{-3}$	$8.4\,10^{-3}$	$4.3\,10^{-3}$	$4.0\,10^{-3}$

Table 5: Comparison between the formation energy of the 9R phase, $E_{form} = E_{coh,R} - E_{coh,c}$, with $E_{coh,R}$ and $E_{coh,c}$ obtained from the simulations (tables 1 and 2) and $E_{form}^{(mod)}$ obtained from the model (equation 2).

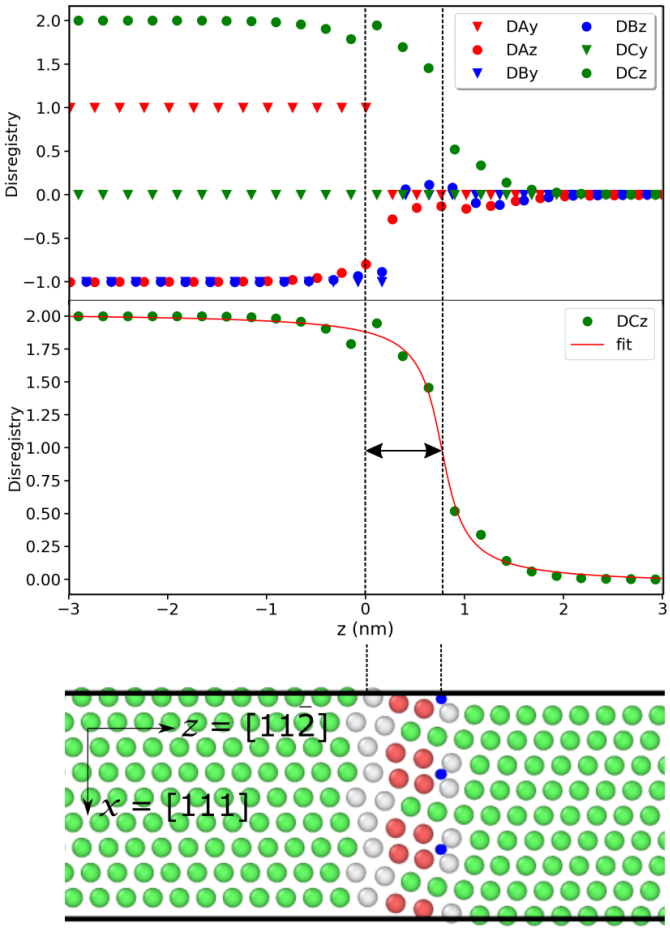

Figure 7: Disregistry analysis for the Foiles potential: a) normalized disregistry versus the position z in δA, δB and δC (111) glide planes. The indexes y and z denote respectively screw and edge components. (b) DCz curve with its fit by an arctangent function. (c) Relaxed ITB atomic structure with atoms coloured according to their CNA parameter (same color code as in figure 4) and localization of the dislocations cores (blue dots) using the DXA (Dislocation Extraction Algorithm) of OVITO.

Table 5 presents the comparison between the results obtained using this model when $\gamma_{int-ISFs}$ is neglected and the results provided by the simulations. We observe that the model gives values of the same order of magnitude as simulations, the differences coming from the interaction energy between the ISFs. These values suggest that the modulus of the interaction energy between ISFs is comparatively large for the Baskes potential, for which the difference between E_{form} obtained from the simulation and $E_{form}^{(mod)}$ obtained from the model is the largest. For the Foiles and Grochola potentials, the interaction energy between the ISFs is so small that, within the uncertainties of the calculations, there is no difference between the obtained formation energies. According to our model, the interaction energy between the ISFs is not insignificant for the Ackland and Baskes potentials and for DFT calculations. We note that this correlates well with the description of an ISF as two CTBs on adjacent planes: while γ_{ISF} is very close to $2\gamma_{CTB}$ for the Foiles and Grochola potentials (see tables 1 and 3), the difference for the Ackland and Baskes potentials and for DFT calculations indicates a large interaction between the ISFs. This explains why there is no linear or even monotonic relationship between the 9R phase formation energy and γ_{ISF}.

3.2.3. Lattice parameters and elastic energy of the 9R phase

The description of the 9R phase in terms of an fcc phase with an ISF every three planes, and of an ISF as two CTBs in consecutive planes, allows an estimation of the 9R phase lattice parameter. Indeed, in the ABCBCACAB sequence, the expected value of the c_{0R} lattice parameter (distance along the $[111]_{9R}$ direction[1] for nine (111) planes in the 9R phase) is

$$c_{0R}^{(mod)} = c_{0c} + 12\delta_{CTB} \tag{3}$$

where $c_{0c} = 3\sqrt{3}a_{0c}$ is the same distance in the fcc phase. The obtained values are given in table 6 and compared to the results from the simulations. This model implies that when $\delta_{CTB} > 0$, $c_{0c} < c_{0R}$, which is the case for the potentials of Ackland and Baskes and the DFT calculations, and that when $\delta_{CTB} < 0$, $c_{0c} > c_{0R}$ which happens for the potentials of Foiles and Grochola.

However, the difference in lattice parameters between the two phases is not the main reason for the deformation of the 9R phase. Indeed, when this phase is formed

[1] We recall that $[111]_{9R}$ corresponds to the $[0001]_h$ direction of the bulk hexagonal phase.

through the relaxation of the ITB, the array of dislocations that separate the fcc and 9R phases induces a rotation, and the 9R phase is strained to ensure consistency between its (111) planes and the (111) planes of the fcc phase, as shown in figure 8. Because of the large difference in the volumes occupied by the two phases, it is supposed that the fcc phase is relaxed whereas the 9R phase has to accommodate the mismatch. The strain ε_{xx} is thus determined by

$$\varepsilon_{xx} = \frac{c_{0c}\cos\alpha - c_{0R}}{c_{0R}} \quad (4)$$

where α=13.26° is the theoretical rotation angle. It is found that the 9R phase is highly contracted along $x//[111]$ (see ε_{xx} values in table 6). There is no relaxation of the simulation cell along the $y//[1\bar{1}0]$ direction, so the 9R phase is forced to have the same lattice parameter as the fcc phase along y. The ensuing strain ε_{yy} has also been determined, but its value is much smaller than ε_{xx}. The boundary conditions being free surfaces along the normal to the ITB, the stress components implying the z coordinate vanish and do not consequently contribute to the elastic energy stored in the 9R phase.

Since the stiffness coefficients and the bulk lattice parameters of the 9R phase have been computed (table 2), and the width of the 9R phase ensuing from the ITB relaxation has been determined, we can estimate the elastic energy γ_{elas} per unit surface of the ITB for the four interatomic potentials. Neglecting the component ε_{xy} and supposing that the strain is homogeneous, we obtain

$$\gamma_{elas} = \frac{e_{9R}}{2} C_{ijkl}\varepsilon_{ij}\varepsilon_{kl} \quad (5)$$

with ij and kl being either xx or yy. After a change of coordinates to express the stiffness coefficients of the 9R phase in the x, y, z basis, and using the width of the 9R phase obtained with the disregistry method, this elastic energy is obtained. The values vary between 22 mJ/m^2 (Grochola and Baskes potentials) and 43 mJ/m^2 (Ackland potential), see table 7.

3.2.4. Contributions in the ITB energy and parameters determining the width of the 9R phase

We have estimated in previous subsections the 9R phase formation and elastic energies which contribute to the energy of the relaxed ITB. The ITB energy contains also interfacial energies, and since the two interfaces differ (with the δA and δB dislocations on one side, the δC on the other side), there are two terms γ_{fcc-9R} and γ_{9R-fcc}. Finally, these two interfaces interact with an interaction energy γ_{int}. We thus have the following decomposition:

$$\gamma_{ITB} = \gamma_{form} + \gamma_{elas} + \gamma_{fcc-9R} + \gamma_{9R-fcc} + \gamma_{int}. \quad (6)$$

Note that all these quantities have the dimension of an energy per unit area. In particular, γ_{form} is obtained with:

$$\gamma_{form} = \frac{E_{form} \times e_{9R}}{v_{9R}}. \quad (7)$$

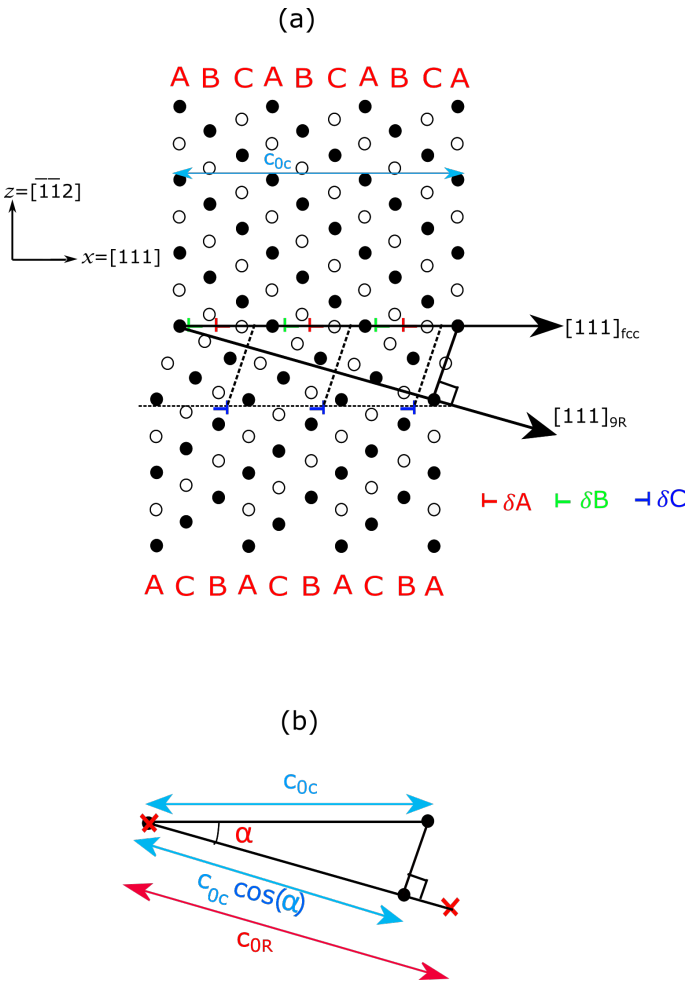

Figure 8: a) [111] directions in the fcc phase and in the 9R phase issued from a relaxed ITB. The angle between $[111]_{fcc}$ and $[111]_{9R}$ is α. b) Representation of the lattice mismatch at the fcc-9R interface as the difference between the two inclined arrows.

	Foiles	Grochola	Ackland	Baskes	GGA	LDA
c_{0R} (Å)	21.18	21.12	21.49	21.24	22.00	21.37
$c_{0R}^{(mod)}$ (Å)	21.19	21.13	21.26	21.18	21.74	21.20
c_{0c} (Å)	21.20	21.15	21.19	21.15	21.67	21.11
ε_{xx} (%)	-2.56	-2.55	-4.06	-3.11	-4.13	-3.85
ε_{yy} (%)	$3.5\,10^{-2}$	$1.6\,10^{-4}$	$-5.1\,10^{-1}$	$-6.7\,10^{-2}$	$5.7\,10^{-1}$	$5.2\,10^{-1}$

Table 6: Lattice parameter along [111] in the 9R phase obtained from simulations (c_{0R}) and from equation 3 ($c_{0R}^{(mod)}$), and the same parameter obtained from simulations in the fcc phase (c_{0c}). Deformations ε_{xx} (equation 4) and ε_{yy} (see text for details).

Using the width of the 9R phase obtained with simulations after the ITB relaxation (table 4, disregistry method), the formation energy and the elastic energy of the 9R phase have been computed in mJ/m^2 to find their contributions in the ITB energy. The results are shown in table 7. We found that the formation energy of the 9R phase (that depends on γ_{ISF} and on the interaction between the ISFs, see equation 2) has a contribution from 1 to 9% of the value of the ITB energy. The contribution of the elastic energy varies from 5 to 8% depending on the potential. Thus, the main contribution to the energy of the ITB comes from the interfacial energies γ_{fcc-9R}, γ_{9R-fcc} and the interaction energy γ_{int} between these two interfaces. This interaction between the two interfaces is necessarily repulsive, otherwise no 9R phase would be formed.

It can be noted that the condition for the expansion of the 9R phase is given by $\partial\gamma_{ITB}/\partial e_{9R} < 0$, which leads to:

$$-\frac{\partial\gamma_{int}}{\partial e_{9R}} > \frac{\gamma_{form}}{e_{9R}} + \frac{\gamma_{elas}}{e_{9R}}, \qquad (8)$$

since γ_{fcc-9R} and γ_{9R-fcc} do not depend on e_{9R}. In the inequality of equation 8, the first member corresponds to the interaction force (per unit surface) between both fcc-9R interfaces and depends on the thickness e_{9R} of the 9R phase. γ_{elas} and γ_{form} being given by equations 5 and 7 respectively, the second member does not depend on e_{9R} and represents the minimum value of the repulsive interaction stress for the 9R phase to expand. Although a full description of the ITB dissociation requires an accurate knowledge of γ_{int} with respect to e_{9R}, the second member of equation 8 can provide good insight in the propensity of the metal to form 9R phase from the ITB dissociation. In this case, it is shown that γ_{form}/e_{9R} and γ_{elas}/e_{9R} are the two main parameters to discuss.

We stated in subsection 3.2.1 that the disregistry method requires choosing which of the dislocations δA or δB separate the 9R and fcc phases. For the Foiles potential for example, this choice induces a variation of 12% in the estimation of the 9R phase width (6.9 Å instead of 7.7 Å). Since the formation and the elastic energies of the 9R phase in the relaxed ITB are proportional to its width, a width of 6.9 Å leads to $\gamma_{form} = 4.7$ mJ/m^2 and $\gamma_{elas} = 25$ mJ/m^2, which changes their contribution to the ITB energy by less than 1%.

We are now in position to discuss the obtained widths of the 9R phase ensuing from the ITB relaxation. They are

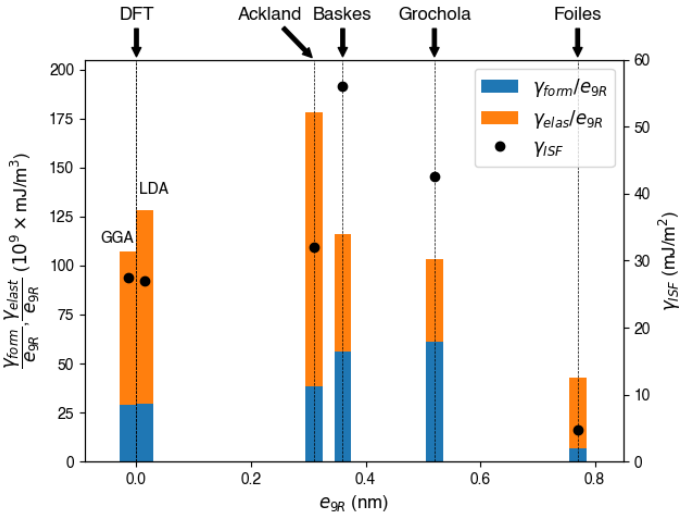

Figure 9: γ_{ISF} (in black), γ_{form}/e_{9R} (in blue) and γ_{elas}/e_{9R} (in orange) versus the width of the 9R phase obtained from the simulations with the disregistry method.

significantly different when estimated with the different potentials. We plot in figure 9 the intrinsic stacking fault energy γ_{ISF}, the 9R phase formation energy γ_{form}/e_{9R} and the elastic energy γ_{elas}/e_{9R} per unit volume versus the width of the 9R phase obtained by the disregistry method for the four interatomic potentials used in this study. It shows that the variations of γ_{ISF} or γ_{form}/e_{9R} as a function of the width of the 9R phase show no clear trend, but the width increases when γ_{elas}/e_{9R} decreases. Indeed, the elastic energy contributes to limiting the extension of the 9R phase. The second member of the equation 8, *i.e.* $\gamma_{form}/e_{9R}+\gamma_{elas}/e_{9R}$, follows the same trend as γ_{elas}/e_{9R}. It has to be noted also that the values of γ_{elas}/e_{9R} and γ_{form}/e_{9R} found in DFT should predict the formation of a 9R phase with a thickness between those obtained with Ackland and Baskes potentials. The absence of 9R phase in DFT calculations might be explained by the additional relaxation mechanism (crystal rotations) not included in our model and certainly due to the reduced sizes considered in such simulations. Focusing on a single material but with potentials leading to different γ_{ISF}, our study emphasizes that the width of the 9R phase cannot be simply related to the stacking fault energy, but that some other parameters have to be taken into account, and suggests that the elastic deformation has a greater influence

	Foiles	Grochola	Ackland	Baskes
γ_{form} (mJ/m^2)	5.2	31.7	12.0	20.1
$\gamma_{form}/\gamma_{ITB}$ (%)	1.3	8.5	2.1	4.6
γ_{elas} (mJ/m^2)	28	22	43	22
$\gamma_{elas}/\gamma_{ITB}$ (%)	7	6	7	5

Table 7: Formation energy in mJ/m^2 and ratio of the formation energy of the 9R phase to the ITB energy; elastic energy in mJ/m^2 (equation 5) and ratio of the elastic energy in the 9R phase to the ITB energy.

on the width of the 9R phase when compared to the other two parameters. This may explain the seemingly contradictory results obtained by Wang and co-workers (decrease of the 9R phase width with γ_{ISF}) [28] and by Gu and co-workers (increase of the 9R phase width with γ_{ISF}) [29]. Finally, we point out that the interfacial energies γ_{fcc-9R} and γ_{9R-fcc} have not been used to discuss the width of the 9R phase because they cannot influence it, though their interaction obviously has an impact.

4. Conclusion

Atomistic simulations have been used in this work to characterize $\Sigma3\{111\}$ CTBs and $\Sigma3\{112\}$ ITBs; their excess volumes and energy densities were obtained. Symmetric ITBs dissociate and an intermediate 9R phase appears. Its width has been studied for many interatomic potentials and with two methods, one accessible experimentally (the angular method), and another one that needs numerical simulations (the disregistry method). The main results obtained in this study can be listed as follows:

- The CTBs and the ITBs introduce an excess volume in the system. Some potentials give positive excess volumes (expansion of the system), while others give negative excess volumes (contraction).
- Contrary to the disregistry method, the angular method is unable to precisely localize the dislocations generating the 9R-fcc and fcc-9R interfaces; this induces uncertainties in the determined width.
- The width of the 9R phase cannot be simply related to the stacking fault energy, some other parameters have to be considered. This may explain the seemingly contradictory results obtained in previous studies.
- The formation energy of the 9R phase can be determined with the intrinsic stacking fault energy, the CTB excess volume and the interaction energy between ISFs. This formation energy contributes to less than 9% to the value of the ITB energy.
- This 9R phase, thin and bounded by two fcc phases is under compressive strain to ensure consistency between the (111) planes of the two phases. The elastic energy contributes to less than 8% to the value of the ITB energy.
- Besides the 9R phase formation and elastic energies, the ITB energy contains the interfacial energies (γ_{fcc-9R} and γ_{9R-fcc}) that cannot affect the width of the 9R phase, and the interaction between these two interfaces. These interfacial and interaction energies have an important contribution compared to the other two. The repulsive interaction between the two interfaces allows the formation of the 9R phase. The latter term should be the subject of a future work.

This works was funded by the French National Research Agency, grant reference ANR-19-CE08-0007. This work also pertains to the French government program "investissements d'Avenir"(LABEX INTERACTIFS, reference ANR-11-LABX-0017-01).

References

[1] L. Lu, Y. Shen, X. Chen, L. Qian, K. Lu, Ultrahigh strength and high electrical conductivity in copper, Science 304 (5669) (2004) 422–426. doi:10.1126/science.1092905.
URL https://www.science.org/doi/abs/10.1126/science.1092905

[2] L. Lu, X. Chen, X. Huang, K. Lu, Revealing the maximum strength in nanotwinned copper, Science 323 (5914) (2009) 607–610. doi:10.1126/science.1167641.
URL https://www.science.org/doi/abs/10.1126/science.1167641

[3] O. Anderoglu, A. Misra, H. Wang, F. Ronning, M. F. Hundley, X. Zhang, Epitaxial nanotwinned Cu films with high strength and high conductivity, Appl. Phys. Lett. 93 (8) (2008) 083108. doi:10.1063/1.2969409.
URL https://aip.scitation.org/doi/abs/10.1063/1.2969409

[4] X. Guo, Y. Xia, Repulsive force vs. source number: Competing mechanisms in the yield of twinned gold nanowires of finite length, Acta Mater. 59 (6) (2011) 2350–2357. doi:10.1016/j.actamat.2010.12.031.
URL https://www.sciencedirect.com/science/article/pii/S1359645410008633

[5] H. Y. Song, Y. Sun, Effect of coherent twin boundary and stacking fault on deformation behaviors of copper nanowires, Comput. Mater. Sci. 104 (2015) 46–51. doi:10.1016/j.commatsci.2015.03.052.
URL https://www.sciencedirect.com/science/article/pii/S0927025615002256

[6] U. Wolf, P. Gumbsch, H. Ichinose, H. F. Fischmeister, Incoherent $\sum$ 3 grain boundaries in fcc metals : the influence of inclinaison on the boundary structure and energy, J. Phys. Colloq. 51 (1990) C1–359–C1–366. doi:10.1051/jphyscol:1990157.
URL http://dx.doi.org/10.1051/jphyscol:1990157

[7] U. Wolf, F. Ernst, T. Muschik, M. W. Finnis, H. F. Fischmeister, The influence of grain boundary inclination on the structure and energy of $\sum = 3$ grain boundaries in copper, Philos. Mag.

A 66 (6) (1992) 991–1016. doi:10.1080/01418619208248003.
URL https://doi.org/10.1080/01418619208248003

[8] D. L. Olmsted, S. M. Foiles, E. A. Holm, Survey of computed grain boundary properties in face-centered cubic metals: I. Grain boundary energy, Acta Mater. 57 (13) (2009) 3694–3703. doi:10.1016/j.actamat.2009.04.007.
URL https://www.sciencedirect.com/science/article/pii/S1359645409002274

[9] A. P. Sutton, R. W. Balluffi, Overview no. 61 on geometric criteria for low interfacial energy, Acta Metall. 35 (9) (1987) 2177–2201. doi:10.1016/0001-6160(87)90067-8.
URL https://www.sciencedirect.com/science/article/pii/0001616087900678

[10] J. Wang, N. Li, A. Misra, Structure and stability of $\sum 3$ grain boundaries in face centered cubic metals, Philos. Mag. 93 (4) (2013) 315–327. doi:10.1080/14786435.2012.716908.
URL https://doi.org/10.1080/14786435.2012.716908

[11] A. D. Banadaki, S. Patala, A simple faceting model for the interfacial and cleavage energies of $\sum 3$ grain boundaries in the complete boundary plane orientation space, Comp. Materials Science 112 (2016) 147–160. doi:10.1016/j.commatsci.2015.09.062.
URL https://www.sciencedirect.com/science/article/pii/S0927025615006436

[12] J. Humberson, I. Chesser, E. A. Holm, Contrasting thermal behaviors in $\sum 3$ grain boundary motion in nickel, Acta Mater. 175 (2019) 55–65. doi:10.1016/j.actamat.2019.06.003.
URL https://www.sciencedirect.com/science/article/pii/S1359645419303623

[13] J. Wang, N. Li, O. Anderoglu, X. Zhang, A. Misra, J. Y. Huang, J. P. Hirth, Detwinning mechanisms for growth twins in face-centered cubic metals, Acta Mater. 58 (6) (2010) 2262–2270. doi:10.1016/j.actamat.2009.12.013.
URL https://www.sciencedirect.com/science/article/pii/S1359645409008556

[14] L. Liu, J. Wang, S. K. Gong, S. X. Mao, High resolution transmission electron microscope observation of zero-strain deformation twinning mechanisms in Ag, Phys. Rev. Lett. 106 (17) (2011) 175504. doi:10.1103/PhysRevLett.106.175504.
URL https://link.aps.org/doi/10.1103/PhysRevLett.106.175504

[15] N. Lu, K. Du, L. Lu, H. Q. Ye, Motion of $1/3\langle 111\rangle$ dislocations on $\sum 3$ {112} twin boundaries in nanotwinned copper, J. Appl. Phys. 115 (2) (2014) 024310. doi:10.1063/1.4861868.
URL https://aip.scitation.org/doi/abs/10.1063/1.4861868

[16] L. Xu, D. Xu, K. N. Tu, Y. Cai, N. Wang, P. Dixit, J. H. L. Pang, J. Miao, Structure and migration of (112) step on (111) twin boundaries in nanocrystalline copper, J. Appl. Phys. 104 (11) (2008) 113717. doi:10.1063/1.3035944.
URL https://aip.scitation.org/doi/abs/10.1063/1.3035944

[17] D. L. Medlin, G. H. Campbell, C. B. Carter, Stacking defects in the 9R phase at an incoherent twin boundary in copper, Acta Mater. 46 (14) (1998) 5135–5142. doi:10.1016/S1359-6454(98)00164-5.
URL https://www.sciencedirect.com/science/article/pii/S1359645498001645

[18] F. Ernst, M. W. Finnis, D. Hofmann, T. Muschik, U. Schönberger, U. Wolf, M. Methfessel, Theoretical prediction and direct observation of the 9R structure in Ag, Phys. Rev. Lett. 69 (4) (1992) 620–623. doi:10.1103/PhysRevLett.69.620.
URL https://link.aps.org/doi/10.1103/PhysRevLett.69.620

[19] D. Hofmann, F. Ernst, Quantitative high-resolution transmission electron microscopy of the incoherent $\sum 3$ (211) boundary in Cu, Ultramicroscopy 53 (3) (1994) 205–221. doi:10.1016/0304-3991(94)90035-3.
URL https://www.sciencedirect.com/science/article/pii/0304399194900353

[20] G. H. Campbell, D. K. Chan, D. L. Medlin, J. E. Angelo, C. B. Carter, Dynamic observation of the fcc to 9R shear transformation in a copper $\sum = 3$ incoherent twin boundary, Scr. Mater. 35 (7) (1996) 837–842. doi:10.1016/1359-6462(96)00220-5.
URL https://www.sciencedirect.com/science/article/pii/1359646296002205

[21] C. B. Carter, D. L. Medlin, J. E. Angelo, M. J. Mills, The 112 lateral twin boundary in fcc materials, Mater. Sci. Forum 207-209 (1996).
URL https://www.osti.gov/etdeweb/biblio/259485

[22] J. D. Rittner, D. N. Seidman, K. L. Merkle, Grain-boundary dissociation by the emission of stacking faults, Phys. Rev. B 53 (8) (1996) R4241–R4244. doi:10.1103/PhysRevB.53.R4241.
URL https://link.aps.org/doi/10.1103/PhysRevB.53.R4241

[23] D. L. Medlin, S. M. Foiles, D. Cohen, A dislocation-based description of grain boundary dissociation: application to a 90° $\langle 110\rangle$ tilt boundary in gold, Acta Mater. 49 (18) (2001) 3689–3697. doi:10.1016/S1359-6454(01)00284-1.
URL https://www.sciencedirect.com/science/article/pii/S1359645401002841

[24] G. Lucadamo, D. L. Medlin, Geometric origin of hexagonal close packing at a grain boundary in gold, Science 300 (5623) (2003) 1272–1275. doi:10.1126/science.1083890.
URL https://www.science.org/doi/abs/10.1126/science.1083890

[25] B. Amin-Ahmadi, H. Idrissi, R. Delmelle, T. Pardoen, J. Proost, D. Schryvers, High resolution transmission electron microscopy characterization of fcc→9R transformation in nanocrystalline palladium films due to hydriding, Appl. Phys. Lett. 102 (7) (2013) 071911. doi:10.1063/1.4793512.
URL https://aip.scitation.org/doi/abs/10.1063/1.4793512

[26] J. Wang, O. Anderoglu, J. P. Hirth, A. Misra, X. Zhang, Dislocation structures of $\sum 3$ {112} twin boundaries in face centered cubic metals, Appl. Phys. Lett. 95 (2) (2009) 021908. doi:10.1063/1.3176979.
URL https://aip.scitation.org/doi/abs/10.1063/1.3176979

[27] J. A. Brown, N. M. Ghoniem, Structure and motion of junctions between coherent and incoherent twin boundaries in copper, Acta Mater. 57 (15) (2009) 4454–4462. doi:10.1016/j.actamat.2009.06.009.
URL https://www.sciencedirect.com/science/article/pii/S1359645409003474

[28] J. Wang, A. Misra, J. P. Hirth, Shear response of $\sum 3\{112\}$ twin boundaries in face-centered-cubic metals, Phys. Rev. B 83 (6) (2011) 064106. doi:10.1103/PhysRevB.83.064106.
URL https://link.aps.org/doi/10.1103/PhysRevB.83.064106

[29] J. Gu, Y. Tang, S. Ni, M. Song, Effect of stacking fault energy on the split length of 9R phase in coarse-grained Cu-Al alloys, Mater. Charact. 142 (2018) 9–14. doi:10.1016/j.matchar.2018.05.021.
URL https://www.sciencedirect.com/science/article/pii/S104458031830500X

[30] D. Hofmann, M. W. Finnis, Theoretical and experimental analysis of near $\sum 3$ (211) boundaries in silver, Acta Metall. Mater. 42 (10) (1994) 3555–3567. doi:10.1016/0956-7151(94)90488-X.
URL https://www.sciencedirect.com/science/article/pii/095671519490488X

[31] S. Plimpton, Fast parallel algorithms for short-range molecular dynamics, J. Comput. Phys. 117 (1) (1995) 1–19. doi:10.1006/jcph.1995.1039.
URL https://www.sciencedirect.com/science/article/pii/S002199918571039X

[32] S. M. Foiles, M. I. Baskes, M. S. Daw, Embedded-atom-method functions for the fcc metals Cu, Ag, Au, Ni, Pd, Pt, and their alloys, Phys. Rev. B 33 (12) (1986) 7983–7991. doi:10.1103/PhysRevB.33.7983.
URL https://link.aps.org/doi/10.1103/PhysRevB.33.7983

[33] G. Grochola, S. P. Russo, I. K. Snook, On fitting a gold embed-

ded atom method potential using the force matching method, J. Chem. Phys. 123 (20) (2005) 204719. doi:10.1063/1.2124667.
URL https://aip.scitation.org/doi/abs/10.1063/1.2124667

[34] G. J. Ackland, G. Tichy, V. Vitek, M. W. Finnis, Simple N-body potentials for the noble metals and nickel, Philos. Mag. A 56 (6) (1987) 735–756. doi:10.1080/01418618708204485.
URL https://doi.org/10.1080/01418618708204485

[35] M. I. Baskes, Modified embedded-atom potentials for cubic materials and impurities, Phys. Rev. B 46 (5) (1992) 2727–2742. doi:10.1103/PhysRevB.46.2727.
URL https://link.aps.org/doi/10.1103/PhysRevB.46.2727

[36] G. Kresse, J. Hafner, Ab initio molecular dynamics for liquid metals, Phys. Rev. B 47 (1) (1993) 558–561. doi:10.1103/PhysRevB.47.558.
URL https://link.aps.org/doi/10.1103/PhysRevB.47.558

[37] G. Kresse, J. Furthmüller, Efficiency of ab-initio total energy calculations for metals and semiconductors using a plane-wave basis set, Comput. Mater. Sci. 6 (1) (1996) 15–50. doi:10.1016/0927-0256(96)00008-0.
URL https://www.sciencedirect.com/science/article/pii/0927025696000080

[38] G. Kresse, J. Furthmüller, Efficient iterative schemes for ab initio total-energy calculations using a plane-wave basis set, Phys. Rev. B 54 (16) (1996) 11169–11186. doi:10.1103/PhysRevB.54.11169.
URL https://link.aps.org/doi/10.1103/PhysRevB.54.11169

[39] J. P. Perdew, K. Burke, M. Ernzerhof, Generalized gradient approximation made simple, Phys. Rev. Lett. 77 (18) (1996) 3865–3868. doi:10.1103/PhysRevLett.77.3865.
URL https://link.aps.org/doi/10.1103/PhysRevLett.77.3865

[40] G. Kresse, D. Joubert, From ultrasoft pseudopotentials to the projector augmented-wave method, Phys. Rev. B 59 (3) (1999) 1758–1775. doi:10.1103/PhysRevB.59.1758.
URL https://link.aps.org/doi/10.1103/PhysRevB.59.1758

[41] A. Stukowski, Visualization and analysis of atomistic simulation data with OVITO–the open visualization tool, Model. Simulat. Mater. Sci. Eng. 18 (1) (2009) 015012. doi:10.1088/0965-0393/18/1/015012.
URL https://doi.org/10.1088/0965-0393/18/1/015012

[42] A. Goyal, Y. Li, A. Chernatynskiy, J. Jayashankar, M. Kautzky, S. Sinnott, S. Phillpot, The influence of alloying on the stacking fault energy of gold from density functional theory calculations, Comp. Mat. Sci. 188 (2021) 110236. doi:10.1016/j.commatsci.2020.110236.

[43] O. Nial, A. Almin, A. Westgren, Röntgenanalyse der systeme gold-antimon und silber-zinn, Z. Phys. Chem. 14B (1) (1931) 81–90. doi:10.1515/zpch-1931-1409.
URL https://www.degruyter.com/document/doi/10.1515/zpch-1931-1409/html

[44] T. J. Balk, K. J. Hemker, High resolution transmission electron microscopy of dislocation core dissociations in gold and iridium, Philos. Mag. A 81 (6) (2001) 1507–1531. doi:10.1080/01418610108214360.
URL https://doi.org/10.1080/01418610108214360

[45] J. R. Neighbours, G. A. Alers, Elastic constants of silver and gold, Phys. Rev. 111 (3) (1958) 707–712. doi:10.1103/PhysRev.111.707.
URL https://link.aps.org/doi/10.1103/PhysRev.111.707

[46] M. Tang, W. C. Carter, R. M. Cannon, Diffuse interface model for structural transitions of grain boundaries, Phys. Rev. B 73 (2) (2006) 024102. doi:10.1103/PhysRevB.73.024102.
URL https://link.aps.org/doi/10.1103/PhysRevB.73.024102

[47] P. Cantwell, T. Frolov, T. Rupert, A. Krause, C. Marvel, G. Rohrer, J. Rickman, M. Harmer, Grain boundary complexion transitions, Ann. Rev. Mater. Res. 50 (2020). doi:10.1146/annurev-matsci-081619-114055.

[48] J. D. Honeycutt, H. C. Andersen, Molecular dynamics study of melting and freezing of small Lennard-Jones clusters, J. Phys. Chem. 91 (19) (1987) 4950–4963. doi:10.1021/j100303a014.
URL https://doi.org/10.1021/j100303a014

[49] D. Faken, H. Jónsson, Systematic analysis of local atomic structure combined with 3D computer graphics, Comput. Mater. Sci. 2 (2) (1994) 279–286. doi:10.1016/0927-0256(94)90109-0.
URL https://www.sciencedirect.com/science/article/pii/0927025694901090

[50] O. Mackain, Modélisation du maclage à l'échelle atomique dans les métaux hexagonaux : germination et migration de disconnections dans le zirconium, le titane et le magnésium, phdthesis, Université de Lyon (2017).
URL https://tel.archives-ouvertes.fr/tel-01591565

[51] A. Kumar, J. Wang, C. N. Tomé, First-principles study of energy and atomic solubility of twinning-associated boundaries in hexagonal metals, Acta Mater. 85 (2015) 144–154. doi:10.1016/j.actamat.2014.11.015.
URL https://www.sciencedirect.com/science/article/pii/S1359645414008593

[52] D. Wolf, Structure-energy correlation for grain boundaries in f.c.c. metals-IV. asymmetrical twist (general) boundaries, Acta Metall. Mater. 38 (5) (1990) 791–798. doi:10.1016/0956-7151(90)90031-B.
URL https://www.sciencedirect.com/science/article/pii/095671519090031B

[53] T. Ma, H. Kim, N. Mathew, D. J. Luscher, L. Cao, A. Hunter, Dislocation transmission across $\sum 3\{112\}$ incoherent twin boundary: a combined atomistic and phase-field study, Acta Mater. 223 (2022) 117447. doi:10.1016/j.actamat.2021.117447.
URL https://www.sciencedirect.com/science/article/pii/S1359645421008260